

Pressure Effect on Mechanical and Electrochemical Properties of Lithium Cobalt Oxide Powder Materials

Qi Liu,^[b, c] Zeqing Duan,^[a] Qiongqiong Qi,^[b] Xiaolu Yang,^{*[b]} Qingshui Xie,^{*[a]} and Jie Lin^{*[a]}

Calender process is important to improve the mechanical and electrochemical properties of cathode materials. To explore pressure effect on structure and resistance of electrode powder, the morphology and surface area of lithium cobalt oxide (LCO) powder under different pressure are investigated. Meanwhile, the real-time stress, density, and conductivity of LCO powder

upon compaction are tested by a self-made detection system. Moreover, the battery performance of LCO powder after compaction is compared in coin cells. This work elucidates the relationship between compaction density, powder resistance, and electrochemical performance of cathode materials for lithium-ion batteries.

1. Introduction

With the rapid development of electrical vehicles (EVs) and smart grids, lithium-ion batteries have been widely used as power sources due to their high energy density, long cycle life, and environmental friendliness.^[1,2] The capacity of widely used lithium-ion batteries (LIBs) is growing rapidly driving the development of up/down-stream industries.^[3] The raw materials for the production of LIBs contain cathode, anode, electrolyte, and polymer separator.^[4] The cathodes are typically manufactured by microscale powder materials which include lithium cobalt oxide (LCO), lithium iron phosphate (LiFePO₄), lithium manganate (LiMn₂O₄), and lithium nickel cobalt manganese oxide (NCM).^[5] Among them, LCO dominates the cathodes for computers, communication, and consumer devices (3 C products) due to the high energy density, high voltage platform, and simple production process.^[6,7] The design and preparation is the most important process for calendering the electrodes.^[8] The electrodes consist of active material, additive, binder, and current collector, increasing the complexity and difficulty of line production for improving the performance of electrodes.^[9] To date, most studies pay attention to directly improve the formation and manufacture of electrodes,^[10–12] but few explore the relationship between compaction process and powder properties.^[13,14] Therefore, it is important to establish a simple method for measuring the powder density and powder conductivity.

The design, fabrication, and treatment of active material powder have huge impact on battery performance.^[15] Through

ball milling, dry powder and slurry are mixed for making electrodes and assembling batteries.^[16] Before mass production, the consistency of active material powder guarantees the stability of battery performance. As an aggregation of particles, the powder properties depend on the components, packing conditions, compressibility, and flowability.^[17] Generally, the particle size of electrode powder is between 1 and 100 microns, and the tiny particles contact with each other. In the mesoscopic scale, the cohesion between the powder and the adhesion with substrates are affected by many factors, which have larger influence on the packing condition than that of particle morphology.^[18] Aggregates or even coherent mass in powder should be avoided to maintain good flowability because the caking of powder leads to partial arching and ratholing resulting in increased resistivity. After the pressurization and depressurization of the upper punch, loose powder is compacted and densified into a cylindrical shape. Electrode powder experiences rearrangement, elastic deformation, plastic deformation, and particle fragmentation in compaction accompanied by changes in mechanical and electrochemical properties.^[19,20] The above mechanisms typically overlap at the same time instead of in sequence. When a compression force is applied on the top of the powder, the void of powder can be reduced from about 40% to 1%, and the relationship between compaction force and compaction density is unclear.^[21] Therefore, it is necessary to investigate the pressure effect on the mechanical and electrical properties of cathode materials.

In this work, the elastoplastic and resistive performance of various LCO powders (Figure 1a) in compaction is studied using a powder resistivity detection system (Figure 1b–d). The real-time stress vs. strain, compaction density, and electrical resistance of LCO powder during loading and unloading are measured by a self-made detection instrument. Moreover, the electrochemical performance of LCO electrodes after various compaction is compared. The material characterizations, compaction, and electrochemical tests reveal the relationship between the various properties of electrode particles.

- [a] Z. Duan, Q. Xie, J. Lin
College of Materials, Xiamen University, 361005 Xiamen, Fujian, China
E-mail: xieqsh@xmu.edu.cn
linjie@xmu.edu.cn
- [b] Q. Liu, Q. Qi, X. Yang
Application Center Lab, Initial Energy Science and Technology, 361000 Xiamen, Fujian, China
E-mail: xiaolu.yang@iesttech.com
- [c] Q. Liu
School of Mechanics and Civil Engineering, China University of Mining and Technology, Xuzhou 221116, China

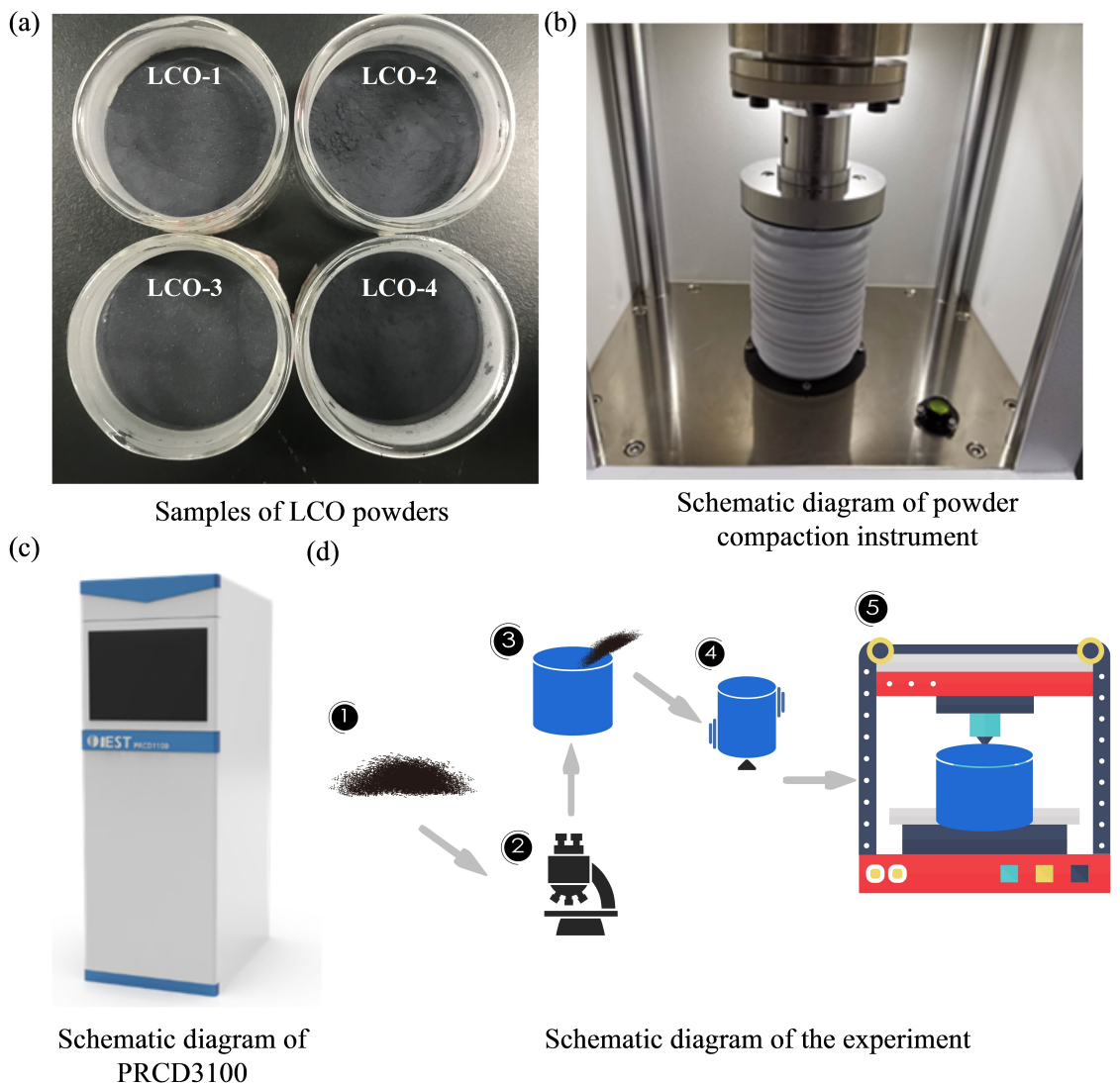


Figure 1. Schematic diagram of experimental materials and instruments: (a) Four LCO samples with a mass of 2 g; (b) Internal diagram of powder compaction detector; (c) External diagram of a powder compaction detector; (d) procedure of powder compaction experiment.

2. Results and Discussion

The SEM images of pristine LCO powder without compaction are shown in Figure 2a-d. No obvious difference can be found in the particle shape. Despite some large particles present in LCO-3, the average particle size of LCO-3 is smaller than LCO-1 as shown in Figure 2e, and the particle size order is LCO-1 > LCO-3 > LCO-2 > LCO-4. The median particle size D_{50} and coefficient uniformity (D_{60}/D_{10}) of powder are obtained to quantify the uniformity of particle size distribution as shown in Figure 2e-h. The specific surface area is in the sequence of LCO-4 > LCO-2 > LCO-1 > LCO-3, which is closely related to the particle size. In summary, the initial material parameters for the LCO powder are listed in Table 1. Most parameters are in the sequence of LCO-1 > LCO-3 > LCO-2 > LCO-4, which could lead to the performance difference below.

Figure 3a-d correspond to the overall and local SEM images of the LCO powders at 50, 100, 150, and 200 MPa, respectively.

The four samples are composed of the LCO particles with the particle size distribution of 36~14, 17~9, 22~11, and 9~4 μm , respectively. The difference in particle size distribution directly affects the filling efficiency, compaction density, and electrochemical properties of the powders during the compression process. Compared with other samples, LCO-4 powders with the smallest average particle size have less particle deformation and are less prone to fragmentation under the same pressure. It can be seen that shear fracture occurs when LCO powder is compacted under a certain force. When the shear stress on any plane is equal to the shear strength of LCO, the surface is cracked. Through the shear fracture process, a set of inclined tensile cracks appear, and as the stress increases, tensile cracks penetrate each other and then form a penetrating shear surface, which ultimately leads to the final shear fracture. It is worth noting that the fracture is only valid for the secondary particles consisting of primary particles.

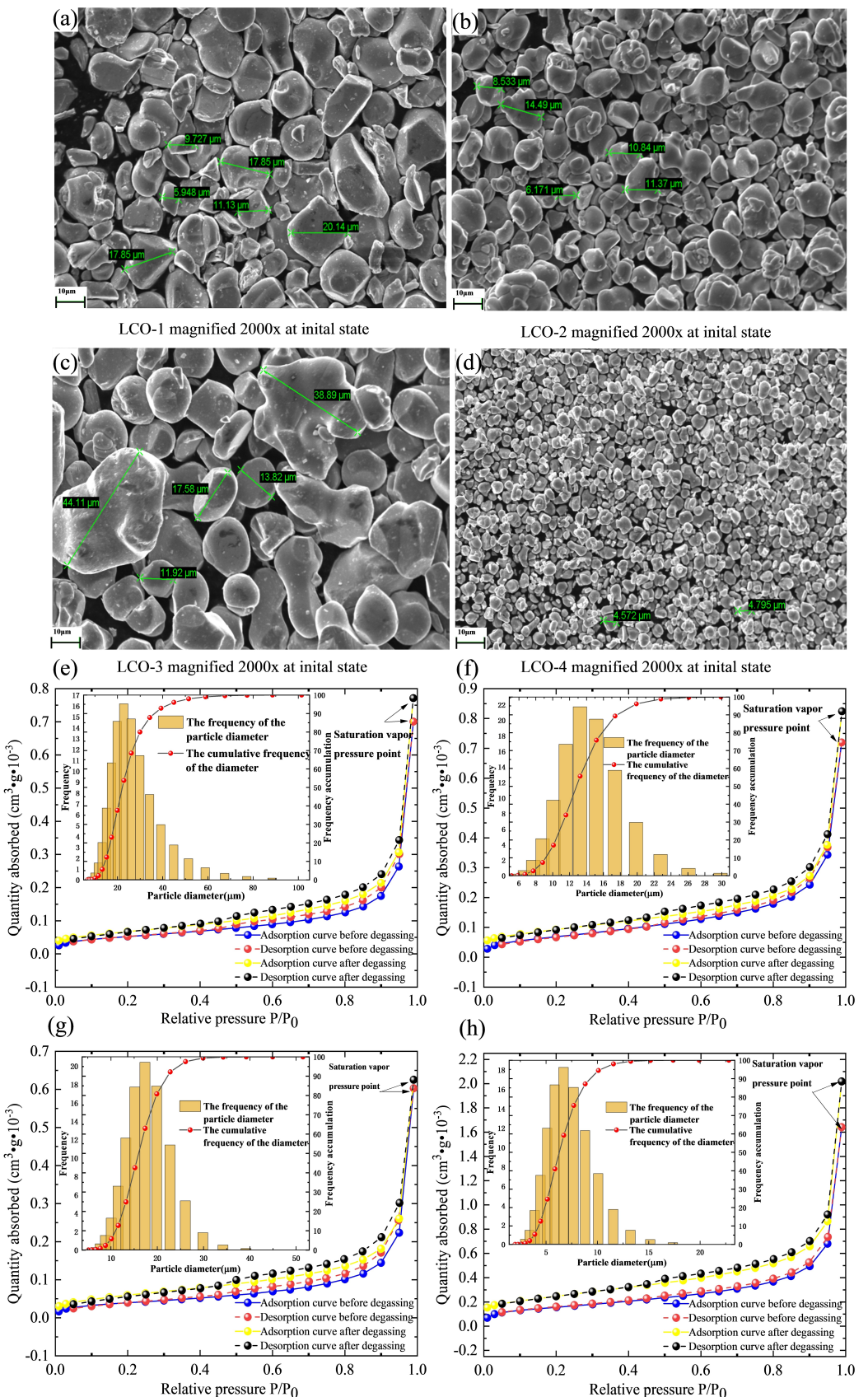


Figure 2. Isothermal adsorption and desorption curves and particle size distribution of LCO powder: (a-d) SEM images of LCO-1 to LCO-4 powder magnified 2000x; (e-h) Gas adsorption and desorption curve and particle size distribution of LCO-1 to LCO-4 at dry room temperature.

Table 1. Initial parameters of LCO samples.

Parameter of powder	LCO-1	LCO-2	LCO-3	LCO-4
Average diameter (μm)	22.08	12.78	18.06	6.27
Pore volume per unit mass (m^3/g)	6.9×10^{-4}	6.44×10^{-4}	4.27×10^{-4}	10.7×10^{-4}
Specific surface area (m^2/g)	0.189	0.254	0.143	0.564
Standard deviation of particle size (μm)	9.64	3.4	4.43	2
Particle size distribution (μm)	14.46~36.31	9.14~17.6	10.96~22.2	4.25~9.29
Vibration density (g/cm^3)	3.1839	2.9498	3.0013	2.0664
Initial void (%)	37.57	42.10	41.15	59.48
Median particle sizes, D_{50} (μm)	22.08185	12.78426	15.93796	6.27334
Coefficient of uniformity, C_u (D_{60}/D_{10})	1.65	1.5	1.61	1.63
Initial resistivity (Ωm)	53.2319	105.1448	458.9851	111.8432
Slope of Heckel curve	0.003618	0.00305	0.003609	0.002657

The self-made system is used to measure the mechanical and electrical properties of powders by applying the loading/unloading compaction (Figure 4a-d). Compaction curves, including compaction density vs. pressure curves, compression cycle curves, stress-strain curves, and Heckel curves are important tools for studying the filling, deformation, and fracture process of electrode powder under compaction. Figure 4a shows a diagram of axial stress and strain for the four LCO samples. The order of maximum deformation and residual deformation is LCO-4 > LCO-1 > LCO-3 > LCO-2. In the loading process, the powder first rearranges, while the compressive stress does not change in the OQ stage. Secondly, in the QA stage, with the increase of compaction, the compaction stress nonlinearily increases to the maximum stress point A. Finally, in the unloading process of AC stage, as is closer to B, the plasticity proportion is greater, and the order is also LCO-4 > LCO-1 > LCO-3 > LCO-2. According to the EEPA theory structure, the stress-strain relationship of LCO can be described as:

$$\sigma_n = \begin{cases} k_1 \varepsilon_n^{1.5} - 2\beta_n \sqrt{m_c} k_1 \varepsilon_n^{0.5} \varepsilon_n \\ k_2 (\varepsilon_n^{1.5} - \lambda \frac{1}{15} \varepsilon_n^{\max}) - 2\beta_n \sqrt{m_c} k_2 \varepsilon_n^{0.5} \varepsilon_n \end{cases} \quad (1)$$

Relative parameters k , β , and m need to be fitted based on the data.

The compaction density vs. stress diagram is plotted in Figure 4b. As the axial stress increases, the compaction density of the LCO powder increases continuously, eventually reaching the ultimate compaction density under the high enough stress. The compaction density of LCO-4 at the same stress is less than that of other specimens, possibly due to the larger initial void and smaller average particle size. At the same time, LCO-3 exhibits the best compaction performance.

For compaction, the porosity-pressure relationship is usually defined by the Heckel equation, which is an empirical formula that summarizes the relationship between compaction stress and density change, expressed as follows:

$$\ln[1/(1-D)] = k\sigma + A \quad (2)$$

Where σ is axial compaction stress and D is the relative density of the powder at a certain σ . k and A are the slopes and intercepts of the fitted straight lines, representing the degree of powder plasticity and the state before deformation, respectively. A larger k value indicates that the density change caused by the same stress change is large, and the plasticity of the powder is great. Experiments show that when k is constant, the relative density change of powder is caused by plastic deformation. If k is a variable, the fitting function is a curve, the change in relative density is caused by factors such as rearrangement, fracture, etc. Figure 4c plots the Heckel curves, fitted straight lines, and differential curves of LCO samples. The k -value order is LCO-4 > LCO-1 > LCO-3 > LCO-2, which means the LCO-4 sample has the smallest average diameter and the largest deformation under the same pressure compared with the other samples. The LCO-2 sample has the least plasticity due to the comprehensive effect. Figure 4d records the data on the thickness and stress of powder over time during compaction. With the loads rising, the internal powder stress gradually increases, while the deformation decreases and approaches the compaction thickness. The LCO-4 sample has the largest plasticity while the other samples show similar elastic-plastic properties.

The total mechanical work W_{total} performed by the upper pouch is represented by the area under the force-displacement curve, which is the sum of the elastic strain energy $W_{elastic}$ and the plastic strain energy $W_{plastic}$. The work is calculated by:

$$W_{total} = W_{plastic} + W_{elastic} = \int F_{load} dh$$

$$W_{elastic} = \int F_{unload} dh \quad (3)$$

Where F_{load} , F_{unload} , and h are loading, unloading force, and axial deformation, respectively. Since the compaction stress increases with the decrease of the upper pouch, the total work performed in the compaction is the area under the compaction curve QA in Figure 4a, i.e. the area enclosed by QAB, where the area enclosed by CAB represents the work done by the elastic recovery of the powder. The total work minus the elastic work to obtain the work done for powder compression molding, i.e. the area enclosed by QAC. The work done for compression

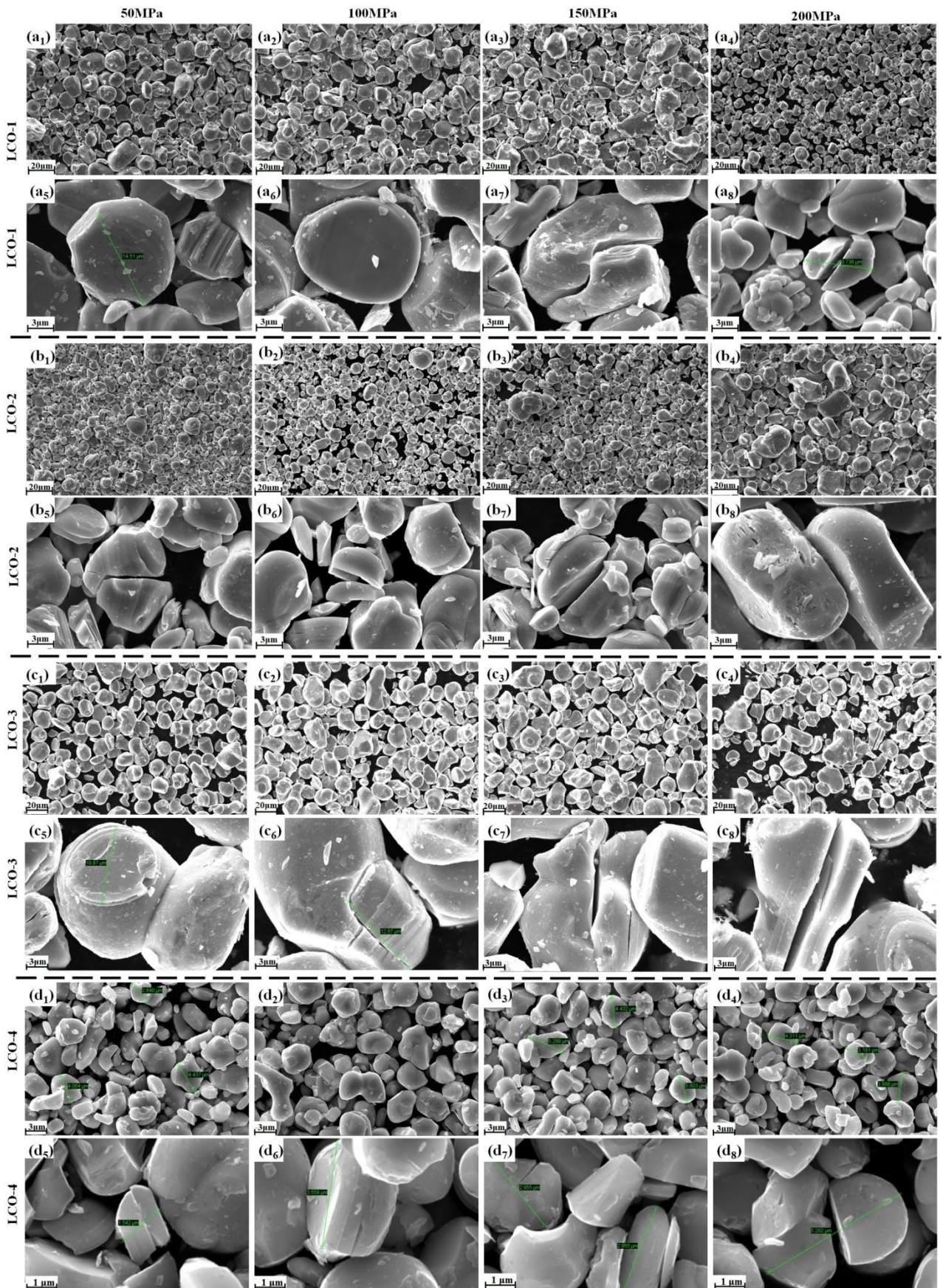


Figure 3. Low and high magnification SEM images of (a₁–a₈) LCO-1, (b₁–b₈) LCO-2, (c₁–c₈) LCO-3, and (d₁–d₈) LCO-4 under different pressures.

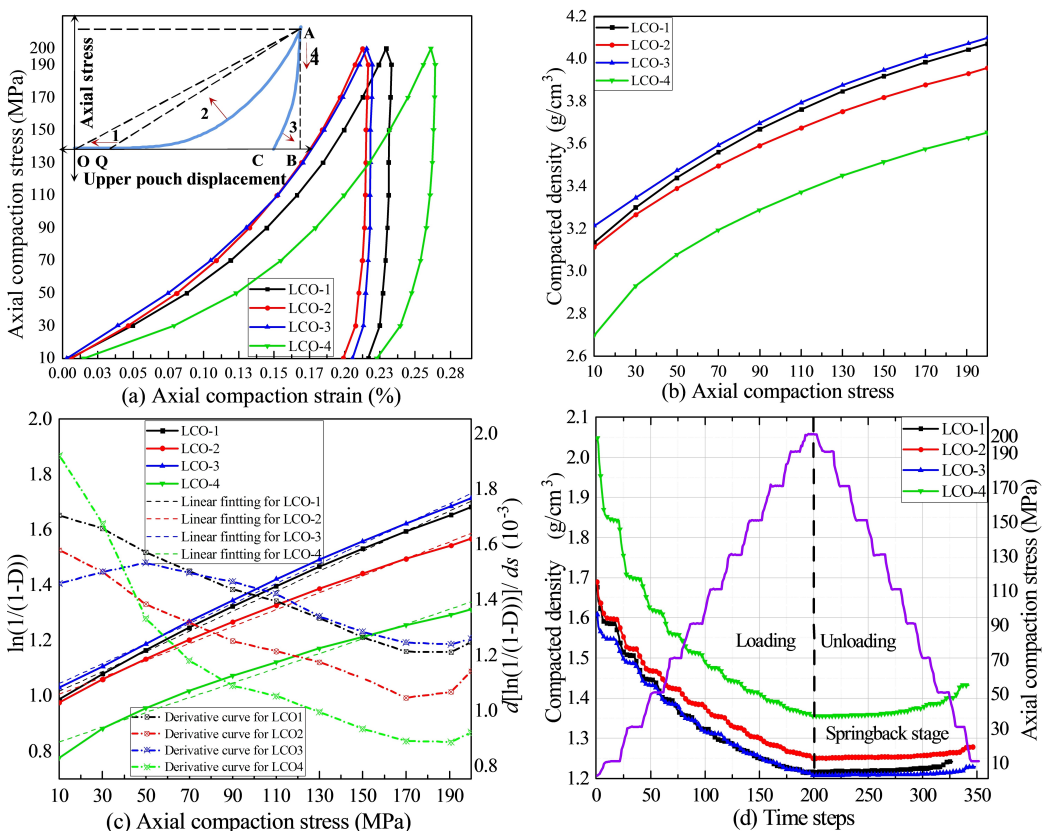


Figure 4. Powder compaction experiments: (a) Axial stress-strain diagram during compaction; (b) Compaction density and axial stress diagram; (c) Axial stress vs. Heckel function/Heckel differential and fit curve diagram; (d) Compaction density and axial stress diagram at different time steps.

molding includes the work done to overcome the friction and repulsion during particle rearrangement, the work done by plastic deformation, the work done for particle fracture, and the work done by friction between the particles and the die. Figure 5a–d show the force-displacement curves and energy ratios of the four LCO samples during compression. It is observed that the LCO-4 with the smallest average diameter has the smallest plasticity ratio. For the specimens with smaller average diameters, reaching the same pressure needs more work, while a major amount of the work done by the pouch is to overcome the friction and repulsion during particle rearrangements, due to the less fracture phenomena during various pressure compaction.

Figure 6a–b show the resistivity and conductivity change during the loading/unloading process, which is computationally reciprocal. With the increase of pressure, the resistivity of LCO powder continues to decrease, and the conductivity order is LCO-3 > LCO-2 ≈ LCO-4 > LCO-1. Figure 6c shows the charge/discharge curves of the LCO-4 sample after being pressed at 50, 100, 150, and 200 MPa. During the first cycle, the LCO electrode under 200 MPa exhibits the highest capacity compared with the other samples due to the close contact between particles. However, the LCO electrode under 200 MPa displays the largely reduced capacity after 200 cycles (Figure 6d) since high pressure leads to particle fragmentation, while the LCO electrode under 50 MPa retains the highest capacity resulting

from the integrated morphology as shown in Figure 3. Meanwhile, the Coulombic efficiency of all samples is retained at ~100% upon cycling implying the full utilization of the active materials. The tests indicate that proper pressure is beneficial to good contact and cycling stability, but too large pressure may lead to the decreased reversible capacity.

3. Conclusions

The mechanical and electrochemical properties of LCO powder are studied by a self-made detection system, which tests the real-time stress-strain, compaction density, and resistivity curves. To some extent, the smaller average diameter leads to larger axial deformation and higher resistivity during compaction, while the compaction density can also be increased. This is because the smaller diameter presents larger specific surface area and less porosity, which could not provide enough void for mechanical deformation. The electrochemical performance of the LCO cathodes after different compaction is mainly affected by the morphology difference, contact area, and electrical conductivity of the powder, indicating that the less pressed LCO electrodes with integrated particles could induce better battery performance.

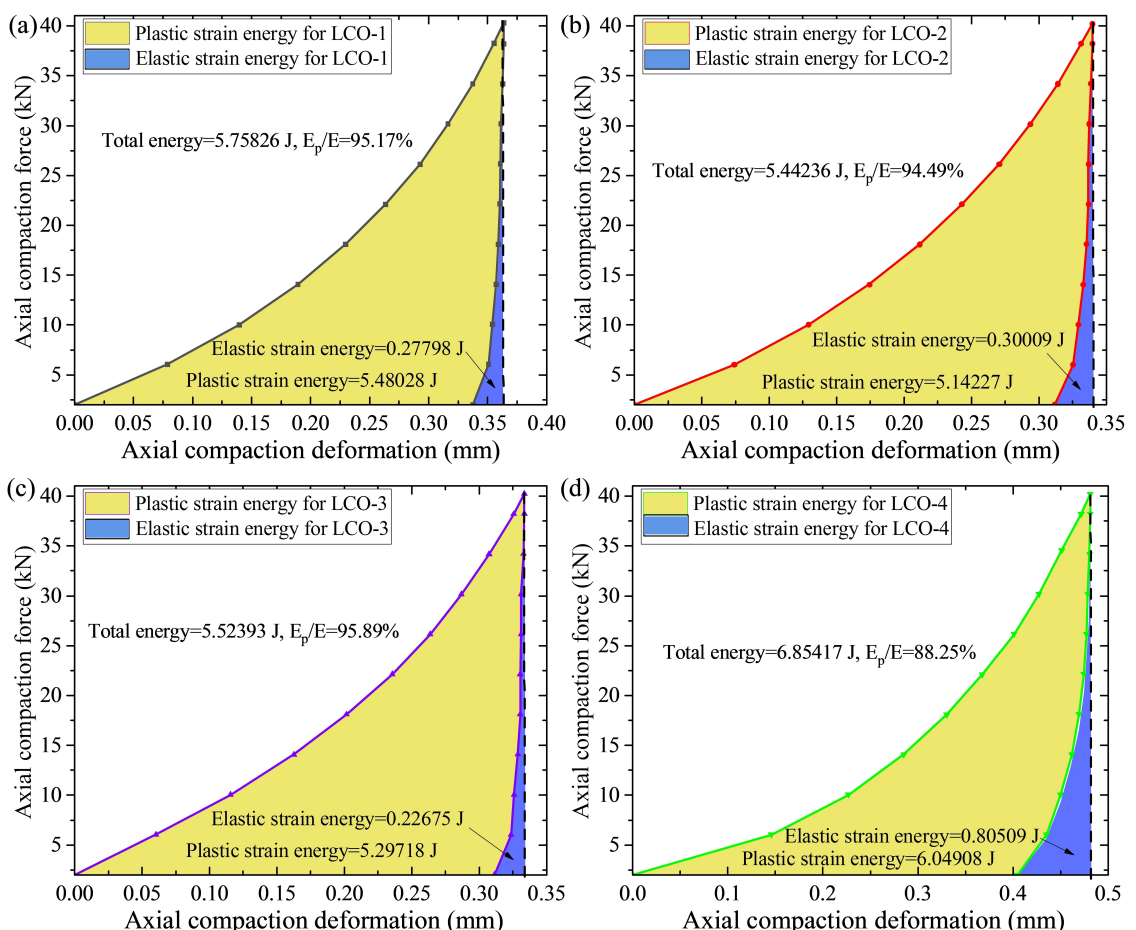


Figure 5. Proportion of elastic and plastic energy of 4 LCO during compression process: (a) Axial displacement and force diagram for (a) LCO-1, (b) LCO-2, (c) LCO-3, and (d) LCO-4 with an elastic-plastic ratio of 95.17%.

Experimental Section

Materials Characterization

A scanning electron microscope (SEM, Zeiss EVO) was used to check the morphology of LCO powder after compaction. The LCO powder was poured into a graduated cylinder and the vibration density was determined by a PF-300B Vibration density meter vibrating 15000 times at a frequency of 250 times per minute. The size distribution of LCO powder was measured by a laser scattering particle size distribution analyzer (LA-960). The inter/intra particle porosity and specific surface area were measured by a Quantachrome instrument.

Compaction Tests

The compaction density and electrical resistivity of the four LCO samples with different particle sizes (Figure 1a) were tested by the self-made detection system (Figure 1b–c), and the average diameter of LCO-1, LCO-2, LCO-3, LCO-4 is 22.08, 12.78, 18.06, and 6.27 μm , respectively. The amount of 2 g LCO powder was weighed out at the same humidity and temperature. As shown in Figure 1 d, the powder was poured into a cylindrical die and placed in the fixture of the detection system. The pressure was applied by the upper pouch ranging from 10 to 200 MPa, increasing by 20 MPa for every 10 seconds, and after reaching 200 MPa, the pressure was decreased at the same unloading rate. Meanwhile, the real-time

compaction density and resistivity change of the powder were recorded by the self-made detection system.

Electrochemical Tests

The LCO powder, acetylene black, and polyvinylidene fluoride (PVDF) were mixed in the mass ratio of 8:1:1 and dissolved in N-methylpyrrolidone (NMP). After drying in a vacuum oven at 90 °C for 12 hours, the LCO-4 electrodes were placed in a roll press and treated with various pressures of 50, 100, 150, and 200 MPa. The electrodes were assembled in CR2025 coin cells inside an argon-filled glove box. The 1 M LiPF₆ dissolved in ethylene carbonate/ethyl methyl carbonate/dimethyl carbonate (EC: EMC: DMC = 1:1:1 in volume) was used as the liquid electrolyte, and the Celgard 2400 was utilized as the separator. The assembled cells were aged for 24 hours before cycling. The constant current charge/discharge tests were conducted on the Neware battery test systems (CT4008Q) at 1 C (first 3 cycles at 0.2 C). All the tests were performed at room temperature.

Highlights

The material properties of lithium cobalt oxide powder after various compaction are investigated. The stress evolution of lithium cobalt oxide powder under pressure is tested by the

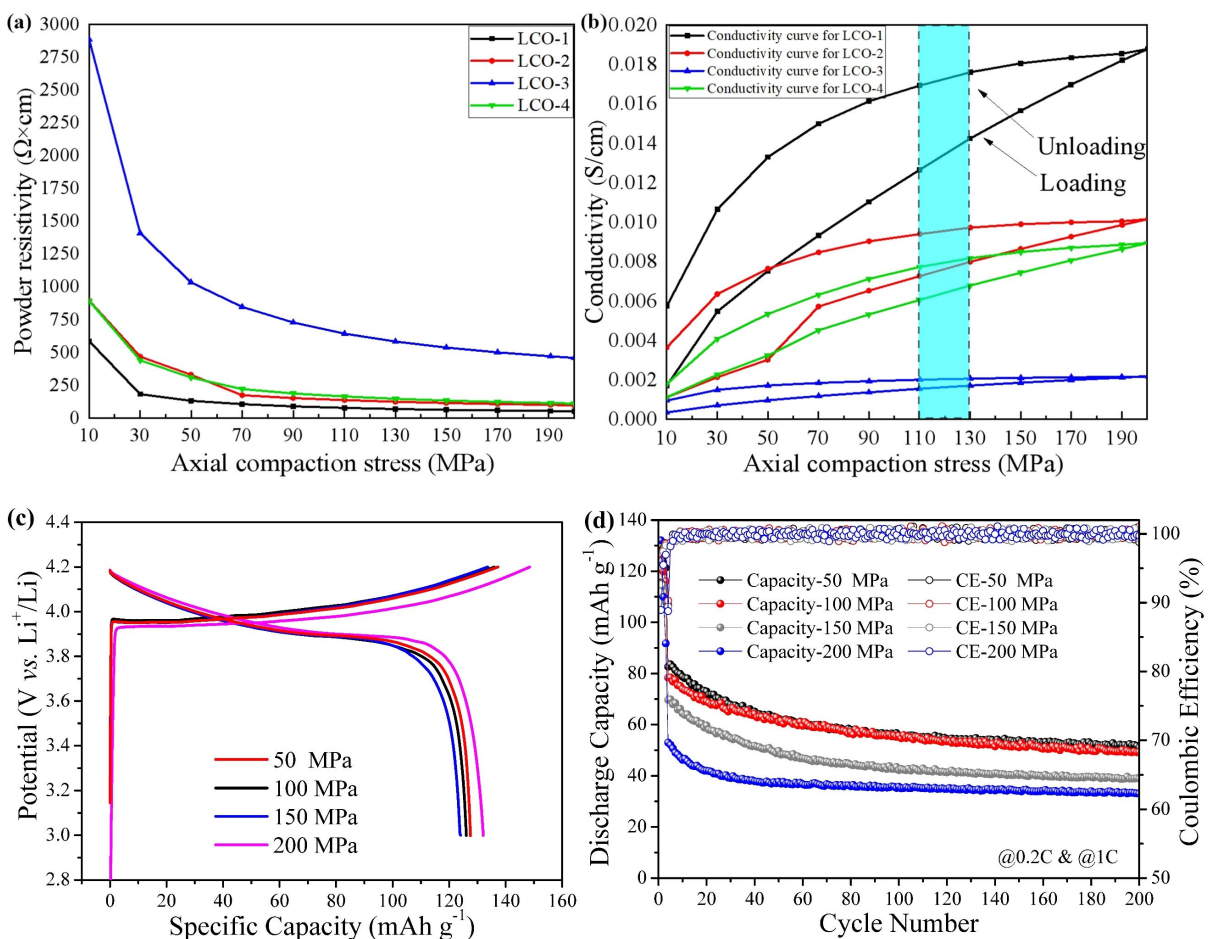


Figure 6. Resistivity, conductivity, and electrochemical properties of LCO powders: (a) Axial stress and powder resistivity diagram upon loading; (b) Axial stress and powder conductivity plots upon loading/unloading; (c) Initial charge/discharge curves of compressed LCO electrodes; (d) Cycling performance and Coulombic efficiency of compressed LCO electrodes.

self-made detector. The real-time conductivity of lithium cobalt oxide powder is measured by the self-made detector. The electrochemical properties of lithium cobalt oxide after various compaction are compared.

Acknowledgements

This work was supported by the National Natural Science Foundation of China (No. 52101273) and Fundamental Research Funds for the Central Universities of China (No. 20720220106). Financial supports from the IEST (Initial Energy Science and Technology) (No. 20223160A0088) are gratefully acknowledged. The experimental setup of PRCD3100 from IEST is also gratefully acknowledged.

Conflict of Interests

The authors declare no conflict of interest.

Data Availability Statement

The data that support the findings of this study are available from the corresponding author upon reasonable request.

Keywords: Lithium cobalt oxide • Compaction • Pressure • Mechanical stress • Electrical conductivity

- [1] C. W. Xiao, B. Wang, D. Zhao, C. H. Wang, *Therm. Sci. Eng.* **2023**, *38*, 101677.
- [2] M. Waseem, M. Ahmad, A. Parveen, M. Suhaib, *J. Power Sources* **2023**, *580*, 233349.
- [3] T. M. Gur, *MRS Bull.* **2021**, *46*, 1153–1163.
- [4] Z. Z. Deng, L. Y. Yang, Y. N. Yang, Z. R. Wang, P. C. Zhang, *Chem. Technol. Fuels Oils* **2022**, *58*, 519–529.
- [5] Y. Ma, *Energy Environ. Mater.* **2018**, *1*, 148–173.
- [6] T. H. Hsueh, C. H. Tsai, S. E. Liu, M. C. Wang, S. M. Chang, A. Shiue, K. Y. Chin, *J. Electrochem. Soc.* **2022**, *169*, 100506.
- [7] Y. T. Liu, R. H. Zhang, J. Wang, Y. Wang, *iScience* **2021**, *24*, 102332.
- [8] N. Sharmili, R. Nagi, P. F. Wang, *J. Energy Storage* **2023**, *68*, 107622.
- [9] P. K. Dammala, K. B. Dermenci, A. R. Kathribail, P. Yadav, J. Van Mierlo, M. Berecibar, *J. Energy Storage* **2023**, *74*, 109209.
- [10] M. F. Niri, G. Apachitei, M. Lain, M. Copley, J. Marco, *Energy Technol.* **2022**, *10*, 2200893.

- [11] A. Diener, S. Ivanov, W. Haselrieder, A. Kwade, *Energy Technol.* **2022**, *10*, 2101033.
- [12] D. Schreiner, J. Lindenblatt, R. Daub, G. Reinhart, *Energy Technol.* **2023**, *11*, 2200442.
- [13] I. de Meatza, I. Landa-Medrano, S. Sananes-Israel, A. Eguia-Barrio, O. Bondarchuk, S. Lijo-Pando, I. Boyano, V. Palomares, T. Rojo, H. J. Grande, I. Urdampilleta, *Batteries* **2022**, *8*, 79.
- [14] M. Wang, K. Uzun, B. R. Frieberg, J. Z. Hu, A. N. T. Li, X. S. Huang, Y. T. Cheng, *J. Electrochem. Soc.* **2023**, *170*, 010541.
- [15] Q. Liu, J. G. Wang, B. W. Hu, *ACS Omega* **2023**, *8*, 7492–7506.
- [16] H. Yang, S. Y. Lin, A. L. Cheng, F. B. He, Z. L. Wang, Y. T. Wu, Y. Zhang, X. Liu, *Energies* **2023**, *16*, 3099.
- [17] S. C. Thakur, H. Ahmadian, J. Sun, J. Y. Ooi, *Particuology* **2014**, *12*, 2–12.
- [18] M. Murtomaa, E. Makila, J. Salonen, *J. Electrost.* **2013**, *71*, 159–164.
- [19] O. Jones-Salkey, Z. Chu, A. Ingram, C. R. K. Windows-Yule, *Pharmaceutica* **2023**, *15*, 1587.
- [20] N. B. Sazali, L. W. Chan, T. W. Wong, *Asian J. Pharm. Sci.* **2023**, *18*, 100794.
- [21] M. Akhilash, P. S. Salini, B. John, T. D. Mercy, *J. Alloys Compd.* **2021**, *869*, 159239.

Manuscript received: June 3, 2024

Revised manuscript received: June 30, 2024

Accepted manuscript online: July 12, 2024

Version of record online: September 5, 2024
